Quantitative assessment of microstructural changes of hydrated cement blends due to leaching and carbonation, based on statistical analysis of image data

Orkun Furat[a,*], Andre Baldermann[b], Claudia Baldermann[c], Martin Dietzel[b], Volker Schmidt[a]

[a] *Institute of Stochastics, Ulm University, 89069 Ulm, Germany*
[b] *Institute of Applied Geosciences (IAG) and NaWi Graz Geocenter, Graz University of Technology, 8010 Graz, Austria*
[c] *Institute of Technology and Testing of Building Materials (IMBT-TVFA), Graz University of Technology, 8010 Graz, Austria*

Abstract

The evolution of the microstructure in corrosive environments plays a key role for the performance and durability of cementitious materials, however, appropriate methods to quantitatively describe microstructural alterations are limited. Here, statistical analysis of microscopic data is used to describe changes in porosity, continuous and individual pore size distributions of reactive cement phases during leaching and carbonation of hydrated cement blends. Therefore, BSE images obtained from (un)damaged areas of the cement blends were segmented using image processing techniques, followed by geometrical characterization and quantitative evaluation of the microstructural response(s). It is shown that the dissolution of portlandite generates a high meso- and macroporosity ($>$ 100-4000 nm pores), whereas precipitation of C-(A)-S-H and Ca-carbonate polymorphs leads to a densification of the microstructure, i.e., reducing the fine meso- and micro-porosity ($<$ 500 nm pores). Cement blends made with hydraulically active SCMs and chemically poorly reactive carbonate fillers performed better than pure (OPC-based) cement paste.

Keywords: Blended cements, Supplementary cementitious materials, Statistical image analysis, Microstructure, Leaching

*Corresponding author
Email address: orkun.furat@uni-ulm.de (Orkun Furat)

1. Introduction

The substitution of ordinary Portland cement (OPC) by supplementary cementitious materials (SCMs) has become common practice in concrete production due to environmental, technical and economic benefits [1, 2, 3, 4]. Nowadays, SCMs like granulated blast furnace slag, metakaolin, fly ash, silica fume, limestone powders and industrial waste products among others are used in concrete at low up to very high levels, e.g., between 10 % and 70 % for cement [5, 6, 7, 8, 9]. Such cement blends have a lower or even negative CO_2 fingerprint than OPC [10] and can exhibit an improved resistance against various physical and chemical attacks, such as freeze-thaw, carbonation, external sulfate attack and leaching [11, 12, 13, 14].

It is well known that the type, amount and composition of SCMs substituted for cement exert an important control on the mineralogy, abundance, distribution and chemical properties (e.g. solubility) of the hydrated cement phases, which in turn define the physical characteristics of the cement paste (e.g. total porosity, pore size distribution and density) and thus the durability properties of the hardened concrete [15, 16, 17, 18]. Substitution of SCMs for cement generally reduces the portlandite content [$Ca(OH)_2$] of a certain mix design, because the SCMs can react with $Ca(OH)_2$ to form calcium-silicate-hydrates (C-S-H phases) during cement hydration (e.g. [19]). C-S-H phases are the principle reaction product in fully hydrated concrete.

Dissolution of $Ca(OH)_2$ and C-S-H phases, for example, via exposure of concrete to soft water (e.g. meteoric water or drainage solutions), leads to an increase in porosity and in a reduction of strength [20, 21, 22, 23]. This weakening of the concrete's microstructural and mechanical properties can subsequently promote a great variety of alteration phenomena, such as Ca-loss and C-S-H phase transformation, alkali-silica reaction, carbonation, de-dolomitization, microorganisms attack, chlorine ingress and/or external sulfate attack [12, 15, 16, 24, 25, 26]. Among these processes mentioned above, a high resistance against leaching attack is arguably one of the most important durability parameter for concrete, if considering that leaching enhances other attack forms [18, 27] and takes place in nearly all man-made and natural surroundings (e.g. [14, 28, 29]).

The substitution of SCMs for cement has a positive effect on the leachability of concrete due to less soluble $Ca(OH)_2$ and denser matrices [30]. The influence of the mix design, type of cement and SCMs used, water/binder ratio, curing time, exposure conditions, etc. on the leachability of OPC-based concrete has been extensively studied (e.g. [21, 31]). Recently, it has been reported in Baldermann et al. [8] that hydrated cement blends with 10 up to 70 wt.% of SCM substitution can exhibit a performance equal or better than OPC-based cement pastes in weakly corrosive environments due to mineralogical and microstructural improvements. However, an advanced knowledge of how these critical parameters affect the material's performance is still limited.

In the present paper, we elucidate microstructural details, such as the development of porosity, continuous and individual pore size distributions as well as the grain size distribution of portlandite, of five hydrated cement blends and of one OPC-based reference mix, previously introduced in Baldermann et al. [8], using an advanced approach based on statistical image analysis of back-scattered electron (BSE) image data to characterize the damage progress in the cement blends. For such a quantitative analysis, image processing algorithms have to be applied on the BSE image data in order to semantically segment the latter into phases or even individual pores and grains [32, 33, 34, 35, 36, 37]. The segmentation of image data depicting the material's microstructure has some advantages over other available pore space characterization methods, such as mercury and Wood's metal intrusion [38, 39, 40], because it allows to compute well-defined descriptors

for characterizing the microstructure's geometry and reactive phase content and distribution [41, 42]. A phase-wise segmentation of image data, e.g., the segmentation into pore space and solid phase, allows for the computation of various informative scalar descriptors, i.e., single numerical values, like porosity, tortuosity and constrictivity [43]. Additionally, functional descriptors like, for example, the continuous pore size distribution or chord length distributions of the pore space can be computed, which provide less aggregated information on the material's phases [44, 45]. Segmenting the phases of image data further into individual objects of interest like pores or grains allows for the computation of size and shape characteristics of each pore or grain [37]. Then, the material can be efficiently analyzed by fitting parametric probability distributions to the histograms of the considered characteristics [46].

Although mathematical procedures and approaches to optimize BSE image qualities and to obtain quantitative porosity data from processed BSE images are commercially available, such standardized results are often not presented at a high level of accuracy, as they frequently do not account for the complexity of the pore space and the mineral phase compositions seen among different sets of samples. Herein, we describe advanced algorithms to compute and interpret the complex distributions of pore spaces and portlandite phase contents across zones of increased vs. decreased chemical reactivity within hydrated cement blends. The presented approach may help to overcome current limitations in the identification of the relations between mineral phase reactivity, alteration mineralogy and corrosion behavior of hydrated cement blends exposed to corrosive CO_2 environments. Therefore, we combine and calibrate well-established conventional algorithms from image processing to compute advanced microstructure descriptors from BSE image data of cement blends. The considered descriptors are used to characterize the evolution of the microstructure of six hydrated cement blends in the course of leaching and carbonation, both qualitatively and quantitatively. Therefore, in Section 2.1 we shortly describe the materials and the imaging procedure which have been considered in Baldermann et al. [8]. The methods from digital image processing utilized for segmenting and analyzing the image data are described in Section 2.2. Then, the microstructure descriptors considered in the present paper which can be computed from the segmented BSE image data, are introduced in Section 2.3. This approach leads to a more detailed probabilistic characterization of pore space and portlandite phase content and relative distribution across the samples. Up to our knowledge, this is the first time where such characterization using functional descriptors has been performed for cementitious materials. The results and a quantitative comparison between the considered hydrated cement blends based on the advanced microstructure descriptors are given in Section 3, where we identify physical and chemical key processes that significantly contribute to the formation of zones of chemical reactivity vs. unreactive or passivated zones. This knowledge can help to better understand the links between mineralogy of hydrated cement blends and the development of alteration patterns upon chemical corrosion. Finally, the microstructural responses of the cement pastes due to combined leaching and carbonation are summarized in Section 4.

2. Materials and methods

2.1. Sample preparation and primary characterization

The mix design of the cement blends, their fabrication, curing and subsequent alteration matrix (i.e. combined leaching and carbonation tests) are described in detail in Baldermann et al. [8]. Briefly, a reference paste (CEM_{100}) made from pure CEM I 52.5R (clinker content: $>$ 95 wt.%;

Table 1: Mix design for the reference cement and cement blends.

Sample	CEM I	SF	MK	MEF	MIF	GS	water	w/p
ID	[cm^3]	[cm^3]	[cm^3]	[cm^3]	[cm^3]	[cm^3]	[cm^3]	[-]
CEM_{100}	159.6						300.6	0.6
CEM_{90}/SF_{10}	143.6	22.8					300.6	0.6
CEM_{90}/MK_{10}	143.6		19.3				300.6	0.6
$CEM_{60}/MEF_{32.5}/MK_{7.5}$	95.7		15.2	60.3			300.6	0.6
$CEM_{60}/MEF_{32.5}/MIF_{7.5}$	95.7			60.3	13.9		300.6	0.6
CEM_{30}/GS_{70}	47.9					120.1	300.6	0.6

C_3A content: 12 wt.%) and five cement blends made from the same cement and containing different amounts and types of SCMs were cast, according to [47, 48]. The cement blends are made of the following SCMs or mixes thereof: silica fume (SF), metakaolin (MK), limestone mesofiller (MEF), limestone microfiller (MIF) and granulated slag (GS). They are labelled as CEM_{90}/SF_{10}, CEM_{90}/MK_{10}, $CEM_{60}/MEF_{32.5}/MK_{7.5}$, $CEM_{60}/MEF_{32.5}/MIF_{7.5}$ and CEM_{30}/GS_{70}, where the indices refer to the percentage of cement which was substituted with the respective SCM (Table 1). These mix designs are currently considered for use in various weakly corrosive environments, such as in underground construction sites, yet their equivalent performance to ordinary Portland-based cements without SCMs has to be proven. The water/powder-ratio (w/p-ratio) was adjusted to 0.6 for all mix designs. The cement pastes were filled into cylindrical plastic tubes (diameter: 70 mm; height: 150 mm) and rotated for 12 h to prevent the specimens from segregation. The total volume of the specimens produced varied from 460 cm^3 to 470 cm^3.

The specimens were immediately transferred into semi-permeable plastic bags which were stored at 100 % relative humidity for a period of 182 days at 20 ± 2 °C to ensure full hydration. Over this timeframe, a thin film of bleed water developed on the specimens' surface which was permanently undersaturated with respect to the partial pressure of CO_2 in atmosphere ($P_{CO_2} = 10^{-3.4}$ atm), causing weakly aggressive leaching of the cement pastes. The subsequent conversion of $CO_{2(1)}$ into dissolved carbon species (mainly $CO_3{}^{2-}$ due to alkaline pore water conditions) induced a further carbonation of the cement pastes and other mineral dissolution and re-precipitation reactions. Specifically, the pore water was at any time close to saturation or undersaturated with respect to portlandite and C-S-H phases of variable type and chemical composition, and highly supersaturated with respect to $CaCO_3$ polymorphs (calcite and vaterite), hydrotalcite [$Mg_6Al_2CO_3(OH)_{16} \cdot 4(H_2O)$] and other AFm phases, such as hydrotalcite (cf. Fig. 2 in reference [8]). These conditions promoted the development of an alteration layer, i.e. a leached, cracked and carbonated zone of variable thickness (0.1 up to 1.5 mm) depending on the mix design of the specimens. On the other hand, the inner zone of the specimens remained unaltered. All materials were subjected to mineralogical, spectroscopic, thermo-analytical and electron-microscopic techniques to study the progress of microstructural damage upon combined leaching and carbonation attack [8]. Important parameters of the altered and unaltered zones of each mix design are provided in Table 2.

2.2. Acquisition and processing of image data

Microscopic alteration features across the specimens were visualized on polished surfaces using backscattered electron (BSE) images (8-10 images for each sample with width: 50 µm and height: 35 µm at a pixel size of 24.4 nm) collected on a Zeiss Sigma 300 VP microscope operated at 15 kV. These image dimensions and numbers of images were chosen to ensure a reasonable degree of

Table 2: Compilation of microstructural properties and reactive phase contents of hydrated cement blends [8].

sample ID	thickness of corrosive layer [µm]	sample description	number of BSE images	porosity [%]	port-landite [%][a]	Ca/Si ratio of C-S-H (molar)[b]	Al/Si ratio of C-S-H (molar)
CEM_{100}	1470 ± 220	unaltered	10	9.5 ± 2	19.7	1.71 ± 0.20	0.12 ± 0.05
		altered	10	23.2 ± 7	17.7	1.23 ± 0.21	0.24 ± 0.09
CEM_{30}/GS_{70}	120 ± 40	unaltered	9	5.7 ± 2	6.2	1.39 ± 0.33	0.37 ± 0.04
		altered	9	6.2 ± 1	6.1	1.16 ± 0.27	0.32 ± 0.06
CEM_{90}/SF_{10}	170 ± 50	unaltered	10	6.9 ± 2	14.5	1.57 ± 0.14	0.14 ± 0.07
		altered	8	9.8 ± 2	13.0	1.21 ± 0.09	0.25 ± 0.08
CEM_{90}/MK_{10}	370 ± 80	unaltered	8	6.4 ± 1	15.9	1.59 ± 0.22	0.31 ± 0.05
		altered	10	5.6 ± 12	12.5	1.32 ± 0.17	0.35 ± 0.06
$CEM_{60}/MEF_{32.5}/MIF_{7.5}$	420 ± 60	unaltered	8	7.3 ± 2	15.5	1.53 ± 0.25	0.16 ± 0.04
		altered	8	8.0 ± 5	14.3	1.34 ± 0.11	0.23 ± 0.08
$CEM_{60}/MEF_{32.5}/MK_{7.5}$	210 ± 40	unaltered	8	6.2 ± 2	8.2	1.56 ± 0.19	0.27 ± 0.11
		altered	8	6.2 ± 3	7.7	1.32 ± 0.16	0.30 ± 0.07

[a]Based on thermogravimetric analyses.
[b]Based on SEM-EDX analyses.

precision and direct comparison of the microstructural properties of the individual samples [49], e.g., after the segmentation described in Section 2.2.3 we observe between 748 an 3291 individual pores in each considered scenario and sample. Moreover, the low standard deviations reported for the porosity in Table 2 indicate a good reproducibility of the data (with the exception of CEM_{90}/MK_{10} (altered)). Mineral identification in the unaltered and altered zones of each mix design was realized by energy dispersive X-ray spectroscopy (single spot analysis at 15 kV; beam diameter: 1-2 µm; acquisition time: 30 s; number of EDX analysis: 3-6 per sample and zone) using an Oxford Instrument X-max^{80} SDD EDXS detector. The analytical precision is better than 2 at.% for Ca, Al and Si analyses [50]. The BSE images allow a quantitative microstructure analysis of the considered cement blends. However, note that the 3D microstructural objects of the blends, like pores or grains, are sampled by means of 2D sections only [51]. According to the instrumental set-up we have chosen the smallest pores to be identified are ∼30-50 nm in size, which is consistent with published literature [8]. Thus, interlayer space in and intragranular porosity of C-S-H phases are not visualized by this approach. A sequence of 8-10 BSE images per sample and zone were considered in the statistical analysis of image data in order (i) to overcome common problems with resin embedding and polishing the surface of the samples and (ii) to obtain a representative picture of the microstructural properties of the individual mix designs. In the following, only the average values are reported unless stated otherwise.

Therefore, the raw BSE image data (see Figure 1a) were processed and semantically segmented such that a differentiation between the material's main mineral phases and the pore space (see also Figure 2 for details) was enabled, i.e., a proper binarization of the image data allows a separation into pore space, primary hydrated cement phases (portlandite and C-S-H phases) and alteration minerals ($CaCO_3$ polymorphs and hydrotalcite), respectively (see Figure 1c).

In Section 2.3, various pore space descriptors are explained which are used to characterize the cement's pore space from the binarized image data like, for example, the porosity or more sophisticated descriptors like the continuous pore size distribution [52, 53]. In addition to the binarization of BSE images, the pore space was further decomposed into individual pores, which allows for an in-depth analysis of the microstructure of the cement blends. Analogously, the main characteristics (area fraction, grain size distribution) of portlandite, i.e., the most reactive hydrated

cement phase, were quantitatively assessed by binarizing and further object-related segmenting the image data. However, note that due to the 2D nature of the image data the computation of some characteristics describing the 3D material is difficult or only possible under certain assumptions, like, for example, stationarity, i.e. spatial statistical homogeneity, and isotropy. Furthermore, some characteristics, like the pore/grain size distribution, computed from 2D sections will be biased towards smaller sizes [51]. Nevertheless, the 2D image data allows for a direct comparison between the cement blends considered in the present paper.

Below, the image processing steps are described, which were performed to enhance and segment the individual BSE images. Therefore, we consider an image I with a resolution of $n \times m$ pixels to be a map $I\colon \mathbb{Z}^2 \to \mathbb{R}$ with $I(x) = 0$ for $x \notin W$, where $W = \{1, \dots, n\} \times \{1, \dots, m\}$ is the sampling window. Then, the (image) value of a pixel at the coordinate $x \in W$ is given by $I(x)$. Note that the microscope is equipped with an Angle Selective BSE (HDAsB) detector using nitrogen as the imaging gas at variable pressures between 10 and 133 Pa, which is ideal for precise boundary, feature and particle measurements at high spatial resolution even in the high vacuum mode (1.2 nm at 15 kV). Nevertheless, there is some noise present in the image data, thus the first image processing step consists of denoising which, however, can blur image features at a small scale.

2.2.1. Image denoising

Denoising of image data can be performed by linear operations, like for example, convolving the image I with a Gaussian kernel [54]. Even though this relatively simple but fast approach can reduce noise significantly, it has the disadvantage of blurring the output image. Therefore, a more sophisticated non-linear operation was used to reduce noise in the image data, namely the so-called non-local means denoising algorithm [55]. Using this method, the values $I_{\text{denoised}}(x)$ of the denoised image I_{denoised} are computed as weighted sums from the original BSE image I, i.e.,

$$I_{\text{denoised}}(x) = \sum_{y \in W} w(x, y) I(y) \quad \text{for each } x \in W. \tag{1}$$

The weight function $w\colon W^2 \to [0, \infty)$ is given by

$$w(x, y) = \frac{1}{Z(x)} \exp\left(-\frac{1}{h^2} \sum_{z \in N} G_\sigma(z) |I(x + z) - I(y + z)|^2 \right), \tag{2}$$

where $N \subset \mathbb{Z}^2$ is a certain (sub-) sampling window centered at the origin $o = (0, 0)$, G_σ is a bivariate Gaussian kernel centered at o with standard deviation σ and covariance $\varrho = 0$, $Z(x)$ is a normalization factor and $h > 0$ is a parameter controlling the degree of smoothing. Results of the non-local means denoising algorithm are visualized in Figure 1b.

2.2.2. Segmentation of the pore space

In order to determine the pore space in image data the smoothed image I_{denoised} has to be binarized, i.e., we compute a new image B_{pore} the pixel values $B_{\text{pore}}(x)$ of which are equal to 0 or 1, where $B_{\text{pore}}(x) = 0$ if $x \in W$ corresponds to the pore space. Therefore, we compute an initial binarization B_{initial} by global thresholding of I_{denoised} with some threshold $T > 0$. For each series of images taken from the individual cement blends the threshold values were manually chosen [56] such that the resulting porosities observed in binarized images were identical to the published

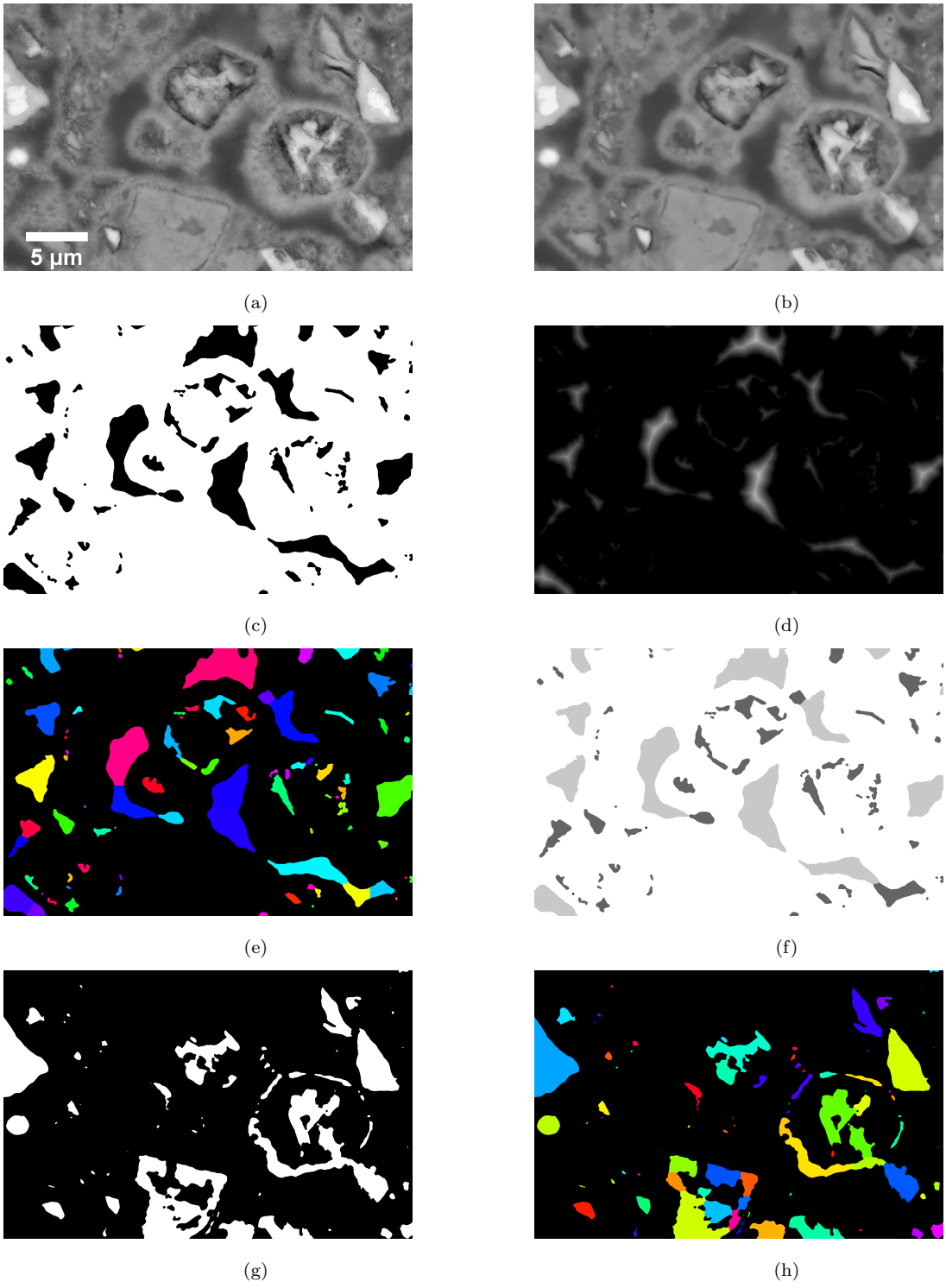

Figure 1: Image processing steps performed to enhance and segment the BSE image data. a: Raw image data. b: Denoised image. c: Binarized image depicting the pore space obtained after global thresholding followed by morphological closing (see Figure 2 for details). d: Euclidean distance transform. e: Segmentation of the pore space into individual pores, where each pore is visualized by its own color. f: Segmentation into solid phase (white), micro- (black), meso- (dark gray) and macropores (bright gray). Due to the resolution of the BSE images micropores below 10-20 nm cannot be depicted properly. g: Binarized image depicting portlandite obtained after global thresholding followed by morphological closing. h: Segmentation of the portlandite phase into individual grains, where each grain is visualized by its own color.

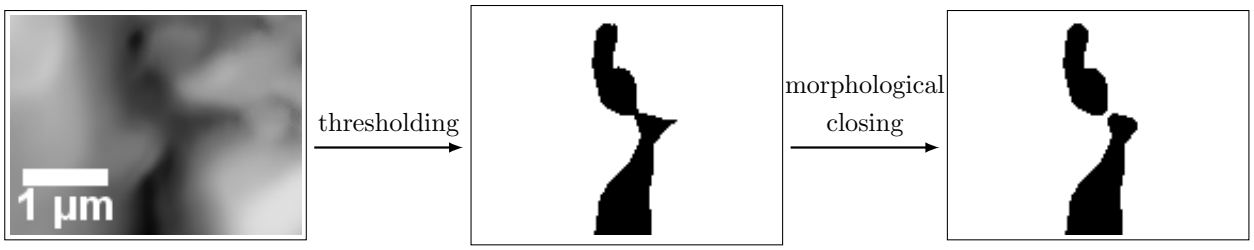

Figure 2: The procedure for binarizing a denoised image I_{denoised} (left). After thresholding the initial binarization B_{initial} (middle) is smoothed by morphological closing in order to obtain the final binarization B_{pore} of the BSE image into solid phase and pore space (right).

porosity data given in Table 2. The results were cross-checked with published X-ray diffraction and thermogravimetric data for verification of accuracy. Figure 2 (middle) depicts the initial binarization B_{initial} which exhibits rather rough boundary lines at the interface between the pore space and the solid phase, where the roughness is caused by noise. In order to reduce this roughness, we use a morphological closing operation with a disk-shaped structural element, the size of which controls the degree of smoothing [35, 57]. Furthermore, the smoothing performed by morphological closing removed small connected components associated with pores which were not distinguishable from noise. Note that too large structural elements may significantly modify characteristics of the binary image data, e.g., the surface area or the number of connected components. The final binarization of the pore phase and the solid phase is depicted in Figure 1c, see also Figure 2 (right).

2.2.3. Segmentation of individual pores

The binarized image B_{pore} allows for an extensive analysis of the pore space. However, it is not yet possible to distinguish individual pores from B_{pore}, since the 2D sections of neighboring pores might be connected in the image data. Consequently, a determination of the size of 2D sections of individual pores is not directly possible. Therefore, we partition the pore space depicted in B_{pore} into individual pores using a marker-controlled watershed algorithm [35, 58], see Figure 1e. The conventional watershed algorithm is a region growth algorithm. It considers a grayscale image I as a topographic map in which, metaphorically speaking, "basins" are filled with "water". The algorithm grows individual basins (regions) starting from local minima of the image I. When two regions touch each other they are separated by a watershed line, resulting in a partition of the image I. Since each local minimum of the image leads to its own region in the segmentation, the conventional watershed algorithm splits, in many applications, the objects of interest into too many regions. This effect is also referred to as oversegmentation. To overcome this issue, we assigned, in a prior step, each object of interest, i.e., each pore, with a single marker. Thus, instead of growing regions from local minima the marker-based watershed algorithm grows them from these predetermined markers. Below, it is described in more detail how the markers are computed for segmenting the pore space.

First, the Euclidean distance transform Ξ of the binary image B_{pore} is computed, which is given by

$$\Xi(x) = \min_{y \in W, B_{\text{pore}}(y)=1} \|x - y\| \quad \text{for each } x \in W, \tag{3}$$

where $\|\cdot\|$ denotes the Euclidean norm. For pixels $x \in W$ associated with the pore space, i.e., with $B_{\text{pore}}(x) = 0$, the value $\Xi(x)$ is the distance from x to the solid phase. If x belongs to the

solid phase, i.e., if $B_{\text{pore}}(x) = 1$, we have $\Xi(x) = 0$. Thus, Ξ is a grayscale image corresponding to the binary image B_{pore}. Note that centers of pores are roughly located at the local maxima of Ξ or equivalently at the local minima of $-\Xi$, see Figure 1d. As mentioned above the watershed algorithm leads to oversegmentation when taking into consideration every local minimum for the region growth procedure. Therefore, we suppress unnecessary minima in $-\Xi$ by computing the so-called h-minima transform [35], from which the local minima are used as markers for the watershed algorithm. The resulting segmentation of the binary image B_{pore} is denoted by S, see Figure 1e for a segmentation of the pore space depicted in Figure 1c into individual pores.

2.2.4. Segmentation of micro-, meso- and macropores

The decomposition of the pore space into individual pores allows to distinguish between different types of pores, i.e., pores can be categorized by their size as micro-, meso- and macropores. Therefore, the areas $A_1, \ldots, A_n$ of each individual pore in S are computed by counting the number of pixels associated with the given pore. Then, the area-equivalent diameters $d_1, \ldots, d_n$ are computed by

$$d_k = \sqrt{\frac{4A_k}{\pi}} \tag{4}$$

for each $k = 1, \ldots, n$. Based on the diameter d_k we define the three types of pores mentioned above. Namely, according to [59], a pore with area-equivalent radius $r_k = d_k/2$ is called

$$\begin{aligned} &\text{micropore,} && \text{if } r_k \leq 100\,\text{nm},\\ &\text{mesopore,} && \text{if } 100\,\text{nm} < r_k \leq 1000\,\text{nm},\\ &\text{macropore,} && \text{if } r_k > 1000\,\text{nm}. \end{aligned}$$

Thus, using these three categories of pores the segmentation S of the binary image B_{pore} can be transformed into an image depicting four phases, namely the solid phase, the micro-, meso- and macropores, see Figure 1f.

2.2.5. Segmentation of the portlandite phase

Similarly to the binarization of the denoised image I_{denoised}, i.e., its decomposition into the pore space and the solid phase described above, we identify the portlandite phase by an additional binarization step. More precisely, using thresholding followed by morphological closing, we compute the binary image B_{port}. For pixels $x \in W$ corresponding to the portlandite phase the image B_{port} has the value 1. Note that the threshold T_{port} (which is larger than the threshold T chosen for the segmentation of the pore space) to determine the portlandite phase within the different zones of the samples was chosen manually, as the z-contrasts between, for example, calcite and portlandite are relatively similar. However, the accuracy of our statistical image analysis was verified by comparison with full-quantitative estimates obtained from X-ray diffraction and TG data (cf. Table 2), and the offset between the datasets turned out to be less than 1 %. For the altered zone of sample CEM_{100} the binary image B_{port} is visualized in Figure 1g. Analogously to the procedure for segmenting the pore space into individual pores, we segment B_{port} into individual portlandite grains using a marker-controlled watershed algorithm, see Figure 1h.

2.3. Statistical analysis of image data

Both the binary image B_{pore} and its segmentation S into individual pores, determined by the approach described in Section 2.2, allow a quantitative characterization of the pore space, which subsequently allows for a quantitative comparison of the microstructural properties of the different hydrated cement blends.

In order to characterize the cement blends using the processed image data considered in Section 2.2, we first investigate the porosity, which is an aggregated pore space descriptor. Then, more complex, functional characteristics are computed, like the continuous pore size distribution and the individual pore size distribution. Furthermore, these characteristics are assessed for each individual type of pores, i.e., for micro-, meso- and macropores. Note that some of the pore space characteristics considered in this paper can be easily transferred to the binary image B_{port} depicting the portlandite phase and its segmentation into individual portlandite grains (see Section 2.2.5). For example, from the binary image B_{port} we can determine the area fraction of portlandite, which is, under the assumption of stationarity and isotropy of the material, equal to its volume fraction in 3D and an analogue of the porosity determined from B_{pore} [60, 61]. Furthermore, the grain size distribution of portlandite grains is determined analogously to the computation of the individual pore size distribution described above.

2.3.1. Porosity

A characteristic pore space descriptor is the porosity ε, which is the area fraction of the pore space in the image data. Note that assuming spatial statistical homogeneity and isotropy of the material, ε is equal to the volume fraction of pore space in 3D. It can easily be estimated from the binary image B_{pore} by

$$\varepsilon = \left(1 - \frac{1}{|W|} \sum_{x \in W} B_{\text{pore}}(x)\right), \tag{5}$$

where $|W|$ denotes the cardinality of the set W, i.e., $|W| = nm$ for an image B_{pore} with a resolution of $n \times m$ pixels. Analogously, the area-fractions of micro-, meso- and macro-pores, i.e., their respective porosities, denoted by $\varepsilon_{\text{micro}}$, $\varepsilon_{\text{meso}}$ and $\varepsilon_{\text{macro}}$, respectively, can be computed.

2.3.2. Continuous pore size distribution

Even though the porosity ε, as a single numerical value, efficiently helps characterizing the pore space, it is a highly aggregated characteristic, i.e., it does not, for example, distinguish between the size and shape of individual pores. Therefore, more sophisticated characteristics of the pore space are computed. One of them is the continuous pore size distribution (CPSD), which provides a functional characterization $F_{\text{cpsd}} \colon (0, \infty) \to [0, 1]$ of the pore space. More precisely, the values of the function F_{cpsd} of a binary image B_{pore} can be determined by

$$F_{\text{cpsd}}(r) = \frac{1}{|W|} \sum_{x \in W} \mathbb{1}_{\Xi(x) > r}, \tag{6}$$

where Ξ is the Euclidean distance transform of B_{pore} given in Equation (3) and $\mathbb{1}$ denotes the indicator function, i.e.,

$$\mathbb{1}_{\Xi(x) > r} = \begin{cases} 1, & \text{if } \Xi(x) > r, \\ 0, & \text{else.} \end{cases} \tag{7}$$

The value $F_{\mathrm{cpsd}}(r)$ of the CPSD given in Equation (6) is the area fraction of that part of the pore space which can be covered by overlapping disks with radius r. The overlapping disks have to be completely contained in the pore space. Note that, contrary to cumulative distribution functions, CPSDs are monotonously decreasing. Furthermore, for infinitesimally small radii r the values of F_{cpsd} converge to the porosity ε, i.e., $\lim_{r\downarrow 0} F_{\mathrm{cpsd}}(r) = \varepsilon$.

2.3.3. Distribution of individual pore sizes

Although the CPSD can easily be computed from the Euclidean distance transform Ξ of the binary image B_{pore} it does not distinguish between individual pores observed in the segmentation given in S, i.e., it does not contain any information regarding the distribution of individual pore sizes. More specifically, the CPSD does not provide a probability density $f\colon \mathbb{R} \to [0,\infty)$ from which we can compute the probability $\mathbb{P}(D \in [a,b])$ of a random pore size D belonging to some interval $[a,b]$ by

$$\mathbb{P}(D \in [a,b]) = \int_a^b f(d)\,\mathrm{d}d. \tag{8}$$

Therefore, in the following it is described how such probability densities can be derived from image data, more specifically, from the area-equivalent diameters $d_1,\ldots,d_n$ of pores computed from the segmentation given in S, see Section 2.2.4. A general parametric approach for modeling the (individual) pore size distribution is exemplarily described for the image data of the unaltered zone of sample CEM_{100}. For the other cases considered in the present paper the modeling has been performed analogously.

The histogram of the area-equivalent diameters $d_1,\ldots,d_n$ observed in the unaltered zone of sample CEM_{100} is visualized in Figure 3. Note that the distribution of pore sizes can be described more efficiently by fitting a parametric probability distribution to the sample $d_1,\ldots,d_n$. More precisely, for a given parametric family of probability densities $\{f_\theta\colon \theta \in \Theta\}$ (e.g., normal, log-normal or gamma distribution) with some set Θ of potentially admissible parameter values, the parameter $\theta_{\mathrm{opt}} \in \Theta$ providing the best fit $f_{\theta_{\mathrm{opt}}}$ is determined by maximizing the (log-)likelihood function L [62], i.e.,

$$\theta_{\mathrm{opt}} = \arg\max_{\theta\in\Theta} L(\theta; d_1,\ldots,d_n), \tag{9}$$

where the likelihood function L is given by

$$L(\theta; d_1,\ldots,d_n) = \prod_{k=1}^{n} f_\theta(d_k). \tag{10}$$

Note that for many parametric families of probability densities there are explicit formulas for computing the optimal parameter θ_{opt}. If no formula is given the optimization problem considered in Equation (9) is solved numerically.

In order to compare various fits obtained for different parametric families of probability densities, we use the Akaike information criterion (AIC) [62] which prefers families with large maximum values $L(\theta_{\mathrm{opt}}; d_1,\ldots,d_n)$ of the likelihood function while keeping the number of model parameters small to avoid overfitting. Thus, using the AIC we choose, among several "common" families of probability densities (namely the Birnbaum-Saunders, Burr, exponential, extreme value, gamma, generalized extreme value generalized Pareto, half-normal, inverse Gaussian, log-logistic, log-normal, Nakagami, Rayleigh, Rician, Weibull distributions [63, 64, 65]), the best parametric fit. Note that

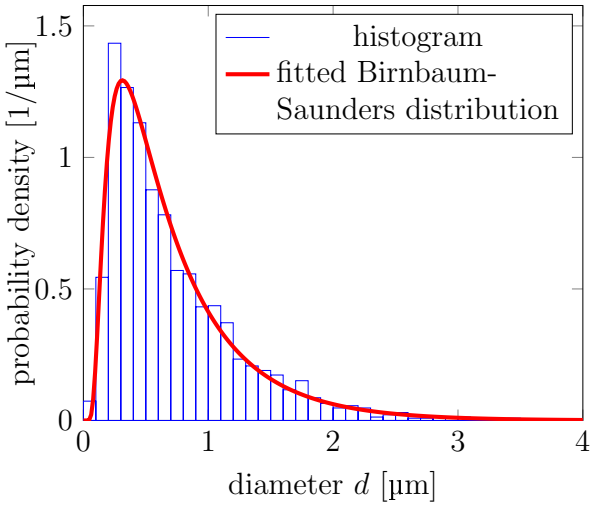

Figure 3: Histogram (blue) of the area-equivalent pore diameters in the unaltered zone of the CEM_{100} samples with a parametrically fitted probability density (red).

the considered families of probability densities are mono-modal which reflects the mono-modality indicated by the histograms of the area-equivalent diameters $d_1, \ldots, d_n$, see, for example, Figure 3 (blue). For example, the Birnbaum-Saunders distribution provides the best fit for describing the probability density of the area-equivalent diameter of pores in the unaltered zone of sample CEM_{100}, see Figure 3.

The probability density f which is fitted to the observed pore diameters $d_1, \ldots, d_n$ (with $n = 2315$) by means of Equation (9) is called a number-weighted probability density [66, 67].

3. Results and discussion

3.1. Quantitative analysis of the pore space

3.1.1. Porosity

In order to determine the porosity of a mix design in either the altered or unaltered zone, $8-10$ BSE images were taken into consideration for each zone of every considered cement blend, each acquired at the same resolution. The porosity of each image was computed by means of Equation (5). For each mix design, the median values of these porosities in the altered and unaltered zone, respectively, were computed to characterize the various mix designs in the respective different zones with a single porosity value each, see Table 2. Analogously, we computed the area-fractions of micro-, meso- and macropores, i.e., their respective porosities, denoted by $\varepsilon_{\text{micro}}, \varepsilon_{\text{meso}}$ and $\varepsilon_{\text{macro}}$. Table 3 lists the median values of the micro-, meso- and macroporosities for the various cement blends in both the unaltered and altered zone considered in the present paper.

The porosity of the materials in the unaltered zone is in the typical range of fully hydrated cement pastes, i.e., varying from $5.7 \pm 2.0\,\%$ to $9.5 \pm 2.0\,\%$ for all mixes [68]. As expected, a reduction of the cement content through addition of SCMs in the cement blends resulted in a sudden decrease of the porosity up to $30\,\%$, compared to CEM_{100}. This is due to an increase of the volume of the hydrated cement phases (especially C-S-H and C-A-S-H) via latent-hydraulic and/or pozzolanic reactions in the presence of hydraulically active SCMs (GS, SF and MK) and/or an increase of the packing density due to a micro-filler effect induced by chemically poorly reactive

Table 3: Median values of the micro-, meso- and macroporosities determined for various cement blends.

	CEM_{100}		CEM_{30}/GS_{70}		CEM_{90}/SF_{10}	
	unaltered	altered	unaltered	altered	unaltered	altered
ε_{micro} [%]	0.0018	0.0019	0.0013	0.0005	0.0020	0.0036
ε_{meso} [%]	6.51	8.61	4.13	3.57	5.94	8.19
ε_{macro} [%]	2.39	12.7	1.73	2.14	0.80	1.94
	CEM_{90}/MK_{10}		$CEM_{60}/MEF_{32.5}/MIF_{7.5}$		$CEM_{60}/MEF_{32.5}/MK_{7.5}$	
	unaltered	altered	unaltered	altered	unaltered	altered
ε_{micro} [%]	0.0064	0.0016	0.0014	0.0011	0.0010	0.0011
ε_{meso} [%]	5.66	5.99	5.23	4.08	3.99	4.29
ε_{macro} [%]	0.21	2.36	1.03	2.99	0.80	3.30

carbonate additives (MEF and MIF) [69, 70]. Comparing the porosities obtained in the altered versus unaltered zone of all mixes it becomes clear that leaching has led to a partially significant increase in the porosity, in particular in sample CEM_{100} (2.2-times), relative to the other mixes. Sample CEM_{90}/SF_{10} exhibited the second-highest increase in porosity (0.7-times), whereas all other mixes remained virtually unaffected or slightly lost porosity (cf. changes in porosity in the altered vs. unaltered zone of each mix reported in Table 2). The comparably high leachability of CEM_{100} and CEM_{90}/SF_{10} is most likely due to the high initial portlandite phase content and high Ca/Si molar ratio of C-S-H in these mixes (Table 2), making their matrices more vulnerable for dissolution processes, which cannot be counterbalanced by their higher degree of carbonation compared to all other mixes (cf. Table 2 in [8]). The competition between leaching-induced gain of secondary porosity versus microstructural densification is evident from the data presented in Table 3: (i) the dissolution of coarser portlandite grains generates a huge meso- and macro-porosity in all mixes, except for sample CEM_{30}/GS_{70}, where this effect is less pronounced due to the relatively lower primary portlandite content (Table 2; [71]). (ii) Ongoing precipitation of hydrated cement phases and fine alteration minerals results in a simultaneous reduction (CEM_{30}/GS_{70} and CEM_{90}/MK_{10}) or stabilization (CEM_{100}, $CEM_{60}/MEF_{32.5}/MIF_{7.5}$ and $CEM_{60}/MEF_{32.5}/MK_{7.5}$) of the micro-porosity despite of progressive leaching action, with the only exception being CEM_{90}/SF_{10}, which gained micro-porosity. The latter, however, is characterized by significant alteration of the C-A-S-H phase composition (cf. Table 3 in [8]), which suggests that the cement matrix of this mix is more vulnerable for leaching attack.

3.1.2. Continuous pore size distribution

Furthermore, the pore space was characterized more extensively with the help of CPSDs. By means of Equation (6), CPSDs were computed from the $8-10$ BSE images for each zone of every considered cement blend. The results are depicted in Figure 4, where the curves were obtained by computing the pointwise median values of the CPSDs of each BSE image obtained from the altered or unaltered zone, respectively. These results indicate that, generally speaking, i.e. in 5 of 6 cases (the only exception being CEM_{30}/GS_{70}), for any radius $r \in [0\,\mu m, 1.5\,\mu m]$ the fraction of the pore space, which can be filled with circles of radius r, is systematically larger in the altered zone.

From these data, three distinct trends can be observed in terms of modification of the pore system: (i) pure cement paste and CEM_{90}/SF_{10} (i.e., made with silica fume) showed a high reac-

tivity, in particular, the finer pores were much more affected than the coarser ones and the porosity gain was generally larger compared to the other mixes (cf. Table 2). This can be attributed to enhanced portlandite leaching and incomplete pozzolanic reaction between microsilica and portlandite, respectively, which retarded a sufficient densification of the microstructure [48]. (ii) Mixes CEM_{90}/MK_{10} and $CEM_{60}/MEF_{32.5}/MK_{7.5}$ (i.e., made with metakaolin) showed a lower porosity gain, but a significant deterioration of the coarser pores compared to all other mixes. A similar negative effect of metakaolin additives was recently observed in Steindl et al. [71] for wet- and dry-mix shotcrete samples subjected to sulfate attack. (iii) In contrast, mixes CEM_{30}/GS_{70} and $CEM_{60}/MEF_{32.5}/MIF_{7.5}$ (i.e., made with granulated slag and limestone) showed a gradual, but much slower shift to a higher porosity and all types of pores were affected in a similar manner. This suggests that enhanced C-(A)-S-H and hydrotalcite formation as well as packing density optimization by addition of slag and fine limestone can improve the leaching resistance of cement blends, corroborating prior findings reported in [3, 71].

3.1.3. Distribution of individual pore sizes

Analogously to the parametric probability density shown in Figure 3, we have fitted the probability densities of the pore sizes for the unaltered and altered zones of each cement blend considered in the present paper, see Figure 5. Comparing the probability densities, it is evident that the mode is typically shifted to the left, i.e., to a smaller pore size, which is due to the microstructural densification described above (CEM_{30}/GS_{70} is the only exception). Dissolution-re-precipitation reactions within the cement matrix and aggregate grains contributed further to changes in the probability densities of the pore sizes, i.e., an increase in the heterogeneity of the different materials is seen, as it can be inferred from the overall "broadening" of the probability density (see red curves in Figure 5). Because probability densities can often be described by just a few parameters, and many characteristics like, e.g., the mean value and the variance can be computed directly from probability densities they are an efficient and informative tool for characterizing materials. More precisely, there are formulas for computing characteristics (mean value, variance etc.) of the distribution from parameters, see [63, 64]. For reproducibility of the results, Table 4 lists the parameters of the fits depicted in Figure 5. Furthermore, the fitted probability densities f allow for the computation of conditional probability densities. For example, from f, we can easily characterize the size distribution of macropores, i.e., pores with an area-equivalent radius larger than 1 µm. More precisely, the probability density f_{macro} of the macropore sizes is given by

$$f_{\text{macro}}(d) = \frac{f(d)}{\int_2^\infty f(x)\,\mathrm{d}x} \quad \text{for each } d > 2. \tag{11}$$

Note that analogously to Equation (11) we can determine the probability densities of micro- and mesopore sizes from f.

3.2. Portlandite phase analysis

As mentioned above, some of the characteristics considered in Section 2.3 for describing the pore space can easily be transferred to the portlandite phase. For example, by substituting B_{pore} with B_{port} in Equation (5) we can compute the portlandite area fractions for the cement blends listed in Table 2.

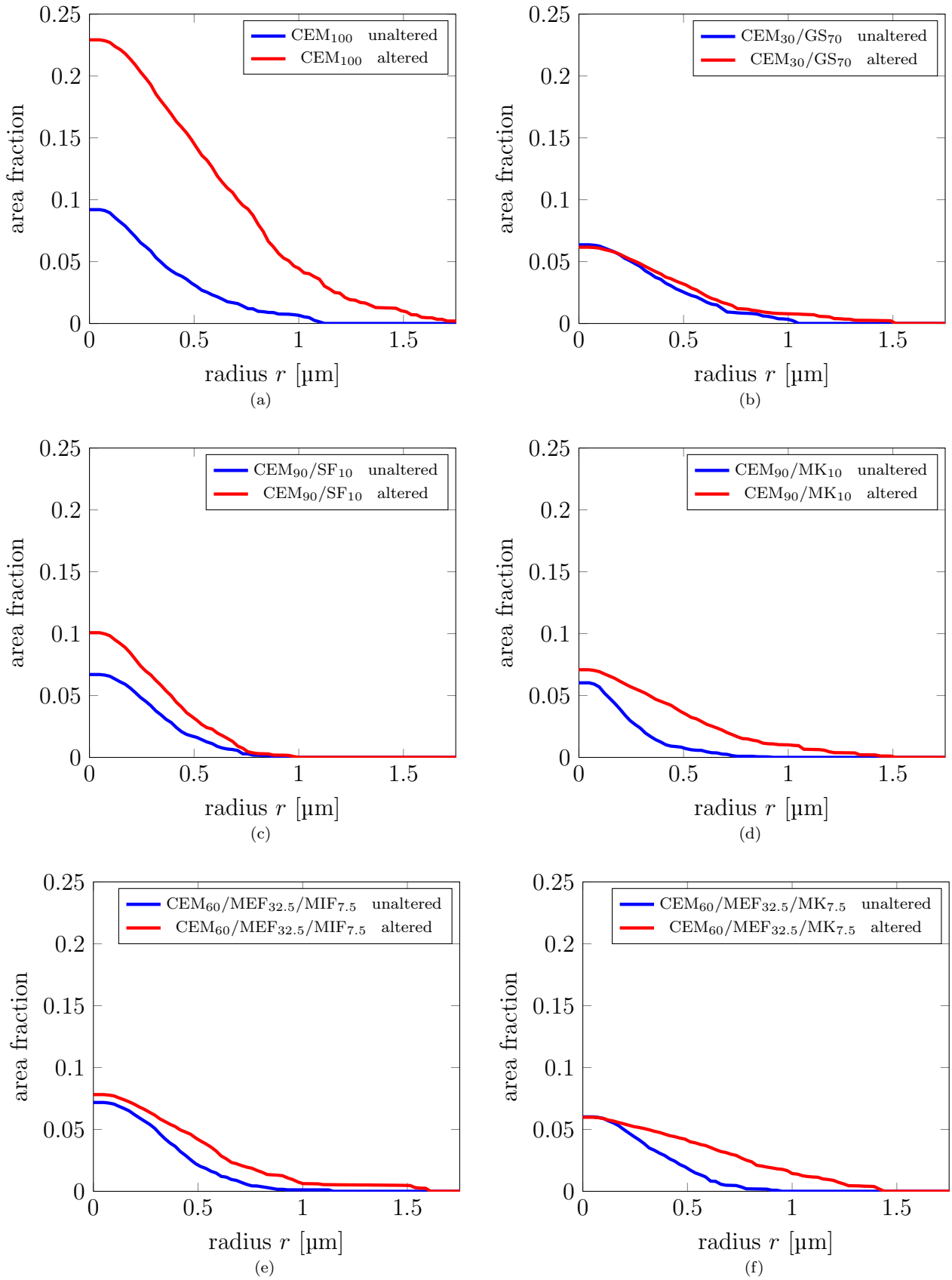

Figure 4: Pointwise median values of the CPSDs computed for the cases listed in Table 2 for the unaltered (blue) and altered (red) zones.

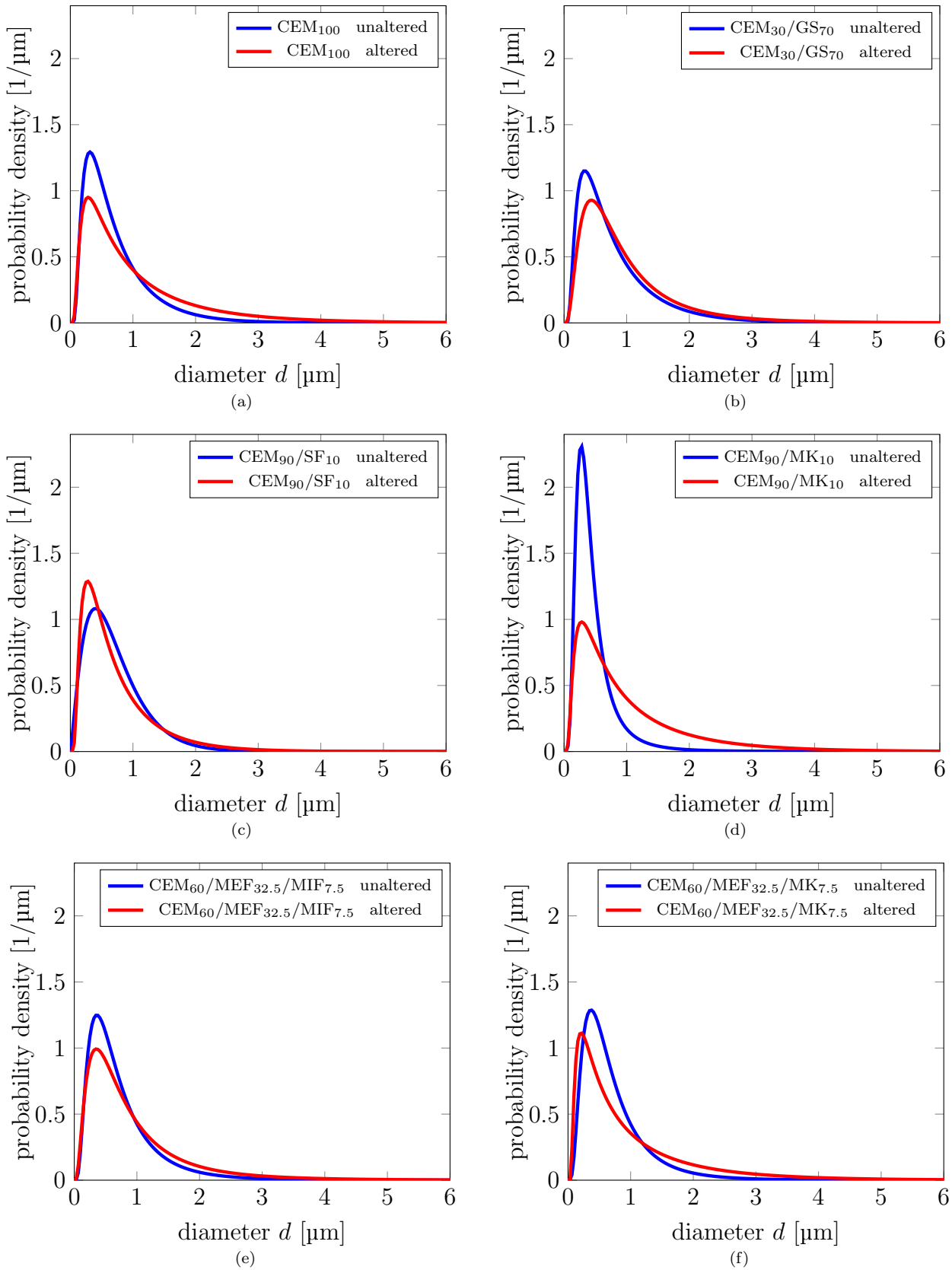

Figure 5: Probability densities of pore sizes of the cement blends listed in Table 2 for the unaltered (blue) and altered (red) zones.

Table 4: Parameters of fitted probability densities describing the pore size distributions depicted in Figure 5. Formulas for these probability densities of the parametric families of distributions can be found in [63, 64].

cement blend	**zone**	**family of distributions**	**parameter values**
CEM_{100}	unaltered	Birnbaum-Saunders	$\beta = 0.56, \gamma = 0.74$
	altered	Birnbaum-Saunders	$\beta = 0.74, \gamma = 0.96$
CEM_{30}/GS_{70}	unaltered	Birnbaum-Saunders	$\beta = 0.63, \gamma = 0.77$
	altered	lognormal	$\mu = -0.27, \sigma = 0.75$
CEM_{90}/SF_{10}	unaltered	gamma	$a = 2.33, b = 0.3$
	altered	Birnbaum-Saunders	$\beta = 0.55, \gamma = 0.81$
CEM_{90}/MK_{10}	unaltered	generalized extreme value	$k = 0.3$, $\sigma = 0.17, \mu = 0.31$
	altered	Birnbaum-Saunders	$\beta = 0.72, \gamma = 0.95$
$CEM_{60}/MEF_{32.5}/MIF_{7.5}$	unaltered	lognormal	$\mu = -0.54$, $\sigma = 0.7$
	altered	lognormal	$\mu = -0.38$, $\sigma = 0.82$
$CEM_{60}/MEF_{32.5}/MK_{7.5}$	unaltered	lognormal	$\mu = -0.55$, $\sigma = 0.67$
	altered	Birnbaum-Saunders	$\beta = 0.65, \gamma = 1.05$

Furthermore, from the segmentation which partitions the binary image B_{port} into individual portlandite grains, see Figure 1h, we compute the area-equivalent diameter of each grain. As described in Section 2.3, we can then fit parametric probability distributions to the extracted grain sizes. The results are visualized in Figure 6. The corresponding families of distributions and parameters are given in Table 5. From these data, two fundamentally different processes can be recognized: (i) The relative increase of portlandite grains with smaller sizes (i.e. $< 0.5\,\mu m$) in the altered zone is interpreted to be due to a relative decrease of the coarser portlandite grains (i.e. 0.5-3.0 µm) through leaching, which also explains the increase in the macro-porosity of most mixes (cf. Figure 5). The only exception is sample CEM_{90}/MK_{10}, probably because of the relatively high amounts of neo-formed carbonates in this mix, which passivated and protected even the coarser portlandite grains from dissolution or conversion to other hydrated cement phases. Similar passivation effects have been described in [1, 3, 18] and are illustrated in Figure 7. (ii) The preservation of the smaller portlandite grains is due to an encapsulation effect induced by the precipitation of volume-expansive hydrated cement phases, i.e., C-(A)-S-H, which prevented the small portlandite grains from further dissolution (cf. Figure 8). It is expected that these portlandite grains will dissolve once the larger portlandite grains have been quantitatively consumed and this process will affect the durability development of the cement blends on the long-term [8, 71].

4. Conclusions

We characterized the evolution of the microstructure of the pore space and the portlandite phase of six different cement blends upon coupled leaching and carbonation, using statistical image analysis based on BSE images of 2D sections of the considered samples. As microstructural descriptors for the modification of the pore space and the reactive phase content, we used the porosity but also functional descriptors like the continuous pore size distribution and the probability density of individual pore sizes. Furthermore, we distinguished between micro-, meso- and macropores which

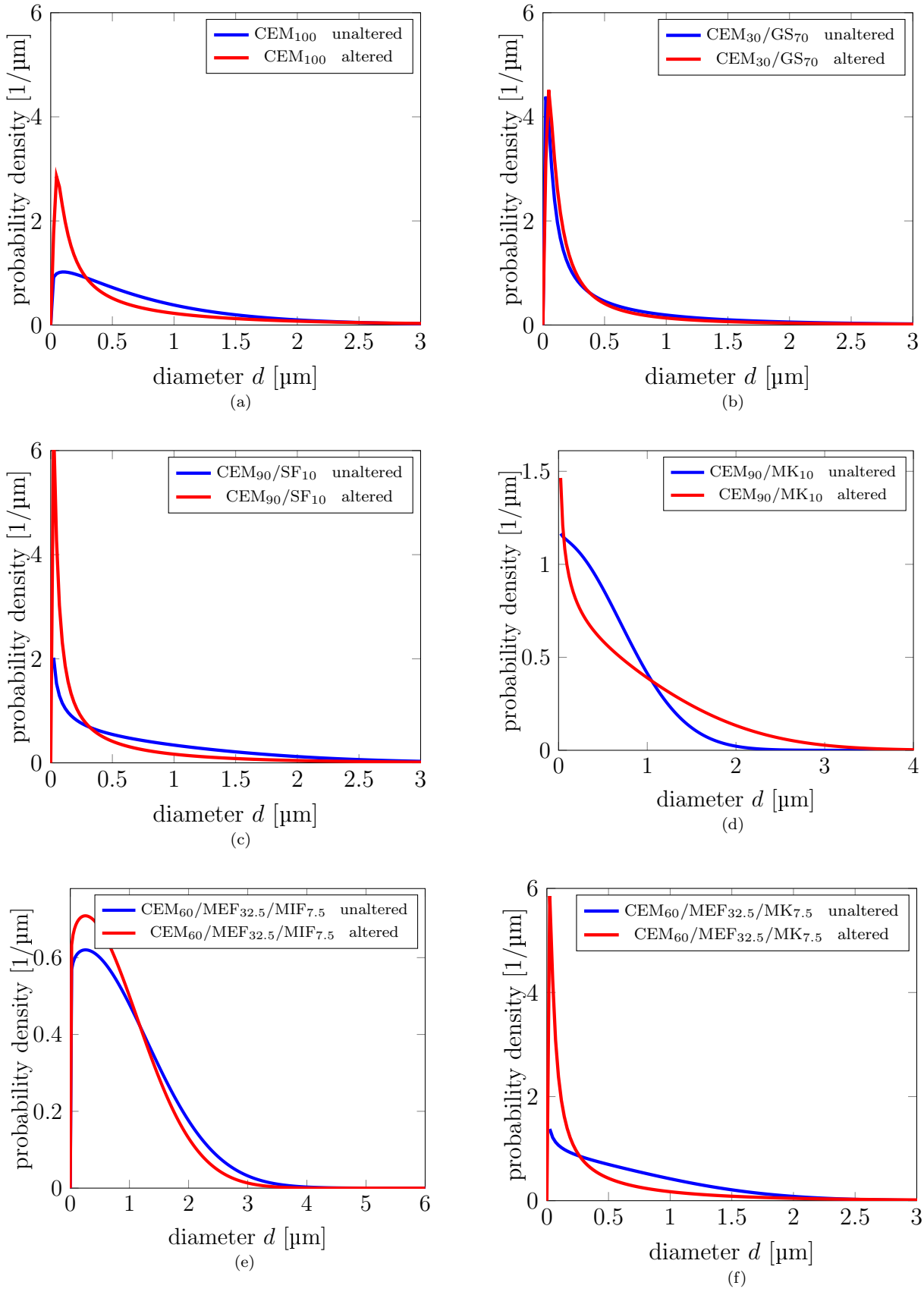

Figure 6: Portlandite grain size distributions of the cement blends listed in Table 2 for the unaltered (blue) and altered (red) zones.

Table 5: Parameters of fitted probability densities describing the grain size distributions depicted in Figure 6. Formulas for the probability densities of these parametric families of distributions can be found in [63, 64].

cement blend	**zone**	**family of distributions**	**parameter values**
CEM_{100}	unaltered	gamma	$a = 1.15, b = 0.68$
	altered	Birnbaum-Saunders	$\beta = 0.32, \gamma = 1.52$
CEM_{30}/GS_{70}	unaltered	Birnbaum-Saunders	$\beta = 0.23, \gamma = 1.67$
	altered	inverse Gaussian	$\mu = 0.48, \sigma = 0.13$
CEM_{90}/SF_{10}	unaltered	Nakagami	$\mu = 0.3, \omega = 1.17$
	altered	Birnbaum-Saunders	$\beta = 0.17, \gamma = 1.81$
CEM_{90}/MK_{10}	unaltered	Nakagami	$\mu = 0.49, \omega = 0.5$
	altered	Nakagami	$\mu = 0.36, \omega = 1.23$
$CEM_{60}/$ $MEF_{32.5}/MIF_{7.5}$	unaltered	Nakagami	$\mu = 0.52, \omega = 1.52$
	altered	Nakagami	$\mu = 0.53, \omega = 1.15$
$CEM_{60}/$ $MEF_{32.5}/MK_{7.5}$	unaltered	Nakagami	$\mu = 0.41, \omega = 0.81$
	altered	Birnbaum-Saunders	$\beta = 0.18, \gamma = 1.74$

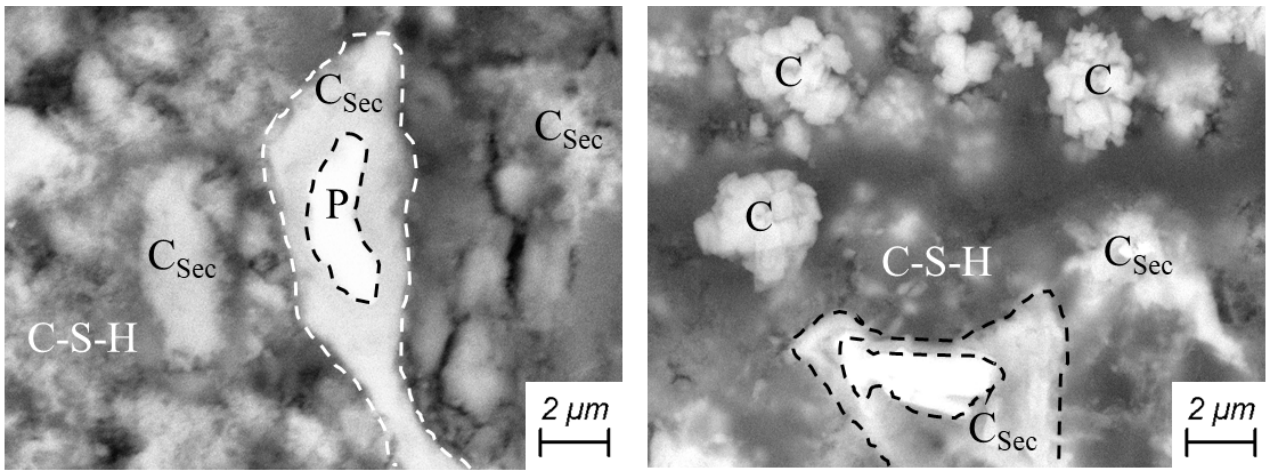

Figure 7: SEM-BSE images of CEM_{90}/MK_{10} (left) and $CEM_{60}/MEF_{32.5}/MK_{7.5}$ (right) showing portlandite grains (P) encapsulated by a thin layer of secondary calcite (C_{Sec}). Note that areas rich in partly carbonated C-S-H phases have a diffuse particle shape vs. primary calcite (C) with a rhombohedral particle shape added as MEF (or MIF)

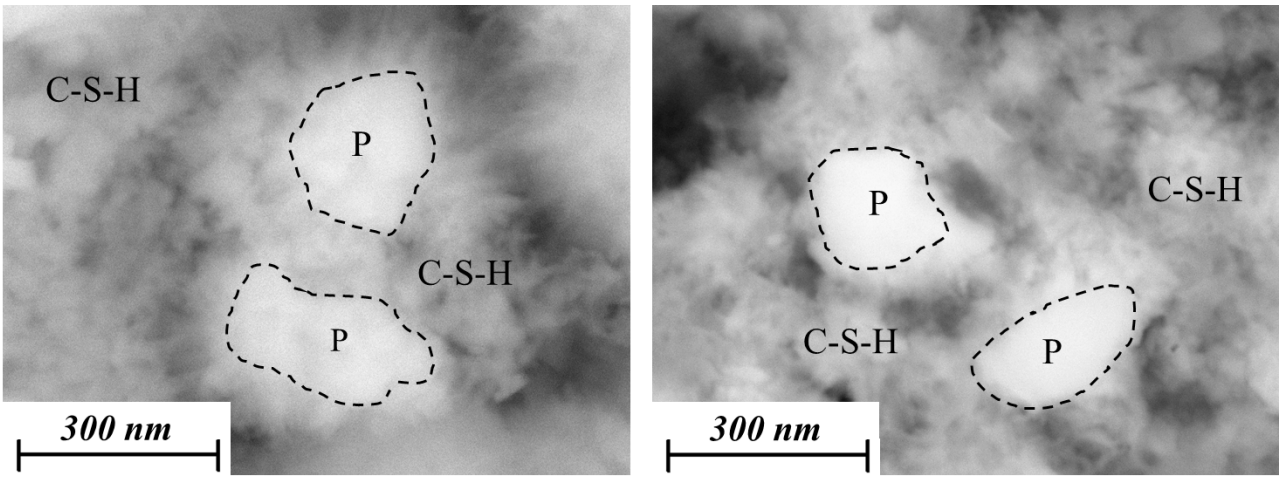

Figure 8: SEM-BSE images of CEM_{90}/MK_{10} (left) and $CEM_{60}/MEF_{32.5}/MK_{7.5}$ (right) showing portlandite grains (P) encapsulated by volume-expansive, fine to foil-like C-(A)-S-H.

allowed the computation of their respective area fractions, i.e., the computation of the micro-, meso- and macroporosity. Moreover, the progress in portlandite phase reactivity of the considered cement blends was characterized by their grain size distributions. These descriptors of the microstructure of the considered cement blends allowed for a detailed analysis of the microstructural changes occurring during leaching and carbonation, which can be summarized as follows:

(i) The reduction of the OPC content by substitution with SCMs (granulated slag, silica fume, metakaolin, limestone, and some of their combinations) led to a decrease in porosity up to 30 %, compared to pure cement paste without additives. Formation of volume-expansive hydrated cement phases (C-S-H and C-A-S-H), prolonged latent-hydraulic and/or pozzolanic reactions and improvements of the packing density due to a carbonate micro-filler effect are the reasons for this porosity reduction.

(ii) Leaching causes a partially significant increase in porosity, depending on the mix design. A severe deterioration of the microstructure was evident in the pure cement paste, compared to the cement blends. Generally, gain in porosity was generated in the meso- and macropore system (>100 nm).

(iii) The dissolution of portlandite grains is responsible for the increase in the meso- and macroporosity. The addition of granulated slag (i.e., sample CEM_{30}/GS_{70}) may reduce this effect, because of a relatively lower primary portlandite content, compared to the other mixes. In contrast, precipitation of C-(A)-S-H, hydrotalcite and Ca-carbonate polymorphs result in a microstructural densification, which is expressed by a decrease in the micro- and fine mesoporosity (<500 nm) in the altered mixes. The only exception is sample CEM_{90}/SF_{10} (i.e., made with silica fume), where the cement matrix was more vulnerable for leaching.

(iv) Carbonation and also C-(A)-S-H phase formation can enhance the passivation of highly reactive hydrated cement phases (i.e., portlandite) via an encapsulation mechanism, which partially prevents the cement matrix from further leaching. This effect is most pronounced in sample CEM_{90}/MK_{10} (i.e., made with metakaolin).

(v) All cement blends made with hydraulically active SCMs and chemically poorly reactive carbonate micro- and meso-fillers showed a better resistance against leaching than pure (OPC-based) cement paste.

References

[1] C. Shi, Z. Wu, J. Xiao, D. Wang, Z. Huang, Z. Fang, A review on ultra high performance concrete: Part I. Raw materials and mixture design, Construction and Building Materials 101 (2015) 741–751. doi:10.1016/j.conbuildmat.2015.10.088.

[2] S. Palm, T. Proske, M. Rezvani, S. Hainer, C. Müller, C.-A. Graubner, Cements with a high limestone content–Mechanical properties, durability and ecological characteristics of the concrete, Construction and Building Materials 119 (2016) 308–318. doi:10.1016/j.conbuildmat.2016.05.009.

[3] A. Baldermann, M. Rezvani, T. Proske, C. Grengg, F. Steindl, M. Sakoparnig, C. Baldermann, I. Galan, F. Emmerich, F. Mittermayr, Effect of very high limestone content and quality on the sulfate resistance of blended cements, Construction and Building Materials 188 (2018) 1065–1076. doi:10.1016/j.conbuildmat.2018.08.169.

[4] D. Patel, R. Shrivastava, R. Tiwari, R. Yadav, Properties of cement mortar in substitution with waste fine glass powder and environmental impact study, Journal of Building Engineering 27 (2020) 100940. doi:10.1016/j.jobe.2019.100940.

[5] B. Lothenbach, K. Scrivener, R. Hooton, Supplementary cementitious materials, Cement and Concrete Research 41 (12) (2011) 1244–1256. doi:10.1016/j.cemconres.2010.12.001.

[6] M. Antoni, J. Rossen, F. Martirena, K. Scrivener, Cement substitution by a combination of metakaolin and limestone, Cement and Concrete Research 42 (12) (2012) 1579–1589. doi:10.1016/j.cemconres.2012.09.006.

[7] E. Aprianti, A huge number of artificial waste material can be supplementary cementitious material (SCM) for concrete production–a review part II, Journal of Cleaner Production 142 (2017) 4178–4194. doi:10.1016/j.jclepro.2015.12.115.

[8] C. Baldermann, A. Baldermann, O. Furat, M. Krüger, M. Nachtnebel, H. Schroettner, J. Juhart, V. Schmidt, J. Tritthart, Mineralogical and microstructural response of hydrated cement blends to leaching, Construction and Building Materials 229 (2019) 116902. doi:10.1016/j.conbuildmat.2019.116902.

[9] Z. E.-A. Laidani, B. Benabed, R. Abousnina, M. K. Gueddouda, E.-H. Kadri, Experimental investigation on effects of calcined bentonite on fresh, strength and durability properties of sustainable self-compacting concrete, Construction and Building Materials 230 (2020) 117062. doi:10.1016/j.conbuildmat.2019.117062.

[10] Z. Ghouleh, R. I. Guthrie, Y. Shao, Production of carbonate aggregates using steel slag and carbon dioxide for carbon-negative concrete, Journal of CO_2 Utilization 18 (2017) 125–138. doi:10.1016/j.jcou.2017.01.009.

[11] M. Romer, L. Holzer, M. Pfiffner, Swiss tunnel structures: concrete damage by formation of thaumasite, Cement and Concrete Composites 25 (8) (2003) 1111–1117. doi:10.1016/S0958-9465(03)00141-0.

[12] F. Mittermayr, A. Baldermann, C. Baldermann, G. H. Grathoff, D. Klammer, S. J. Köhler, A. Leis, L. N. Warr, M. Dietzel, Environmental controls and reaction pathways of coupled dedolomitization and thaumasite formation, Cement and Concrete Research 95 (2017) 282–293. doi:10.1016/j.cemconres.2017.02.011.

[13] B. Słomka-Słupik, J. Podwórny, M. Staszuk, Corrosion of cement pastes made of CEM I and CEM III/A caused by a saturated water solution of ammonium chloride after 4 and 25 days of aggressive immersion, Construction and Building Materials 170 (2018) 279–289. doi:10.1016/j.conbuildmat.2018.03.073.

[14] F. R. Steindl, A. Baldermann, I. Galan, M. Sakoparnig, L. Briendl, M. Dietzel, F. Mittermayr, Chemical resistance of eco-concrete–Experimental approach on Ca-leaching and sulphate attack, Construction and Building Materials 223 (2019) 55–68. doi:10.1016/j.conbuildmat.2019.06.189.

[15] F. P. Glasser, J. Marchand, E. Samson, Durability of concrete—Degradation phenomena involving detrimental chemical reactions, Cement and Concrete Research 38 (2) (2008) 226–246. doi:10.1016/j.cemconres.2007.09.015.

[16] A. Leemann, P. Nygaard, J. Kaufmann, R. Loser, Relation between carbonation resistance, mix design and exposure of mortar and concrete, Cement and Concrete Composites 62 (2015) 33–43. doi:10.1016/j.cemconcomp.2015.04.020.

[17] C. S. Walker, S. Sutou, C. Oda, M. Mihara, A. Honda, Calcium silicate hydrate (C-S-H) gel solubility data and a discrete solid phase model at 25°C based on two binary non-ideal solid solutions, Cement and Concrete Research 79 (2016) 1 – 30. doi:10.1016/j.cemconres.2015.07.006.

[18] I. Galan, A. Baldermann, W. Kusterle, M. Dietzel, F. Mittermayr, Durability of shotcrete for underground support–review and update, Construction and Building Materials 202 (2019) 465–493. doi:10.1016/j.conbuildmat.2018.12.151.

[19] H. F. W. Taylor, Cement Chemistry, Thomas Telford Ltd, 1997.

[20] J. Cowie, F. Glasser, The reaction between cement and natural waters containing dissolved carbon dioxide, Advances in Cement Research 4 (15) (1992) 119–134. doi:10.1680/adcr.1992.4.15.119.

[21] B. Bary, Simplified coupled chemo-mechanical modeling of cement pastes behavior subjected to combined leaching and external sulfate attack, International Journal for Numerical and Analytical Methods in Geomechanics 32 (14) (2008) 1791–1816. doi:10.1002/nag.696.

[22] V. Duong, R. Sahamitmongkol, S. Tangtermsirikul, Effect of leaching on carbonation resistance and steel corrosion of cement-based materials, Construction and Building Materials 40 (2013) 1066–1075. doi:10.1016/j.conbuildmat.2012.11.042.

[23] P. Choi, K.-K. Yun, J. H. Yeon, Effects of mineral admixtures and steel fiber on rheology, strength, and chloride ion penetration resistance characteristics of wet-mix shotcrete mixtures containing crushed aggregates, Construction and Building Materials 142 (2017) 376–384. doi:10.1016/j.conbuildmat.2017.03.093.

[24] C. Grengg, F. Mittermayr, A. Baldermann, M. E. Böttcher, A. Leis, G. Koraimann, P. Grunert, M. Dietzel, Microbiologically induced concrete corrosion: A case study from a combined sewer network, Cement and Concrete Research 77 (2015) 16–25. doi:10.1016/j.cemconres.2015.06.011.

[25] S. P. Arredondo-Rea, R. Corral-Higuera, J. Gómez-Soberón, D. C. Gámez-García, J. Bernal-Camacho, C. Rosas-Casarez, M. Ungsson-Nieblas, Durability parameters of reinforced recycled aggregate concrete: Case study, Applied Sciences 9 (4) (2019) 617. doi:10.3390/app9040617.

[26] E. Boehm-Courjault, S. Barbotin, A. Leemann, K. Scrivener, Microstructure, crystallinity and composition of alkali-silica reaction products in concrete determined by transmission electron microscopy, Cement and Concrete Research 130 (2020) 105988. doi:10.1016/j.cemconres.2020.105988.

[27] M. Rosenqvist, L.-W. Pham, A. Terzic, K. Fridh, M. Hassanzadeh, Effects of interactions between leaching, frost action and abrasion on the surface deterioration of concrete, Construction and Building Materials 149 (2017) 849–860. doi:10.1016/j.conbuildmat.2017.05.137.

[28] D. Jacques, L. Wang, E. Martens, D. Mallants, Modelling chemical degradation of concrete during leaching with rain and soil water types, Cement and Concrete Research 40 (8) (2010) 1306–1313. doi:10.1016/j.cemconres.2010.02.008.

[29] J. Duchesne, A. Bertron, Leaching of cementitious materials by pure water and strong acids (HCl and HNO_3), in: M. Alexander, A. Bertron, N. De Belie (Eds.), Performance of Cement-based Materials in Aggressive Aqueous Environments, Springer, 2013, pp. 91–112. doi:10.1007/978-94-007-5413-3_4.

[30] J. Jain, N. Neithalath, Physico-chemical changes in nano-silica and silica fume modified cement pastes in response to leaching, International Journal of Materials and Structural Integrity 3 (2-3) (2009) 114–133. doi:10.1504/IJMSI.2009.028608.

[31] J. Stark, Recent advances in the field of cement hydration and microstructure analysis, Cement and Concrete Research 41 (7) (2011) 666–678. doi:10.1016/j.cemconres.2011.03.028.

[32] K. Lyu, W. She, C. Miao, H. Chang, Y. Gu, Quantitative characterization of pore morphology in hardened cement paste via SEM-BSE image analysis, Construction and Building Materials 202 (2019) 589–602. doi:10.1016/j.conbuildmat.2019.01.055.

[33] S. Schlüter, A. Sheppard, K. Brown, D. Wildenschild, Image processing of multiphase images obtained via X-ray microtomography: A review, Water Resources Research 50 (4) (2014) 3615–3639. doi:10.1002/2014WR015256.

[34] J. B. Roerdink, A. Meijster, The watershed transform: Definitions, algorithms and parallelization strategies, Fundamenta Informaticae 41 (1, 2) (2000) 187–228. doi:10.3233/FI-2000-411207.

[35] P. Soille, Morphological Image Analysis: Principles and Applications, Springer, 2013.

[36] S. H. Ibrahim, M. Neumann, F. Klingner, V. Schmidt, T. Wejrzanowski, Analysis of the 3D microstructure of tape-cast open-porous materials via a combination of experiments and modeling, Materials & Design 133 (2017) 216–223. doi:10.1016/j.matdes.2017.07.058.

[37] A. Spettl, R. Wimmer, T. Werz, M. Heinze, S. Odenbach, C. Krill III, V. Schmidt, Stochastic 3D modeling of Ostwald ripening at ultra-high volume fractions of the coarsening phase, Modelling and Simulation in Materials Science and Engineering 23 (6) (2015) 065001. doi:10.1088/0965-0393/23/6/065001.

[38] J. Kaufmann, Characterization of pore space of cement-based materials by combined mercury and wood's metal intrusion, Journal of the American Ceramic Society 92 (1) (2009) 209–216. doi:10.1111/j.1551-2916.2008.02834.x.

[39] J. Kaufmann, Pore space analysis of cement-based materials by combined nitrogen sorption–wood's metal impregnation and multi-cycle mercury intrusion, Cement and Concrete Composites 32 (7) (2010) 514–522. doi:10.1016/j.cemconcomp.2010.04.003.

[40] S. Xue, P. Zhang, J. Bao, L. He, Y. Hu, S. Yang, Comparison of mercury intrusion porosimetry and multi-scale X-ray CT on characterizing the microstructure of heat-treated cement mortar, Materials Characterization 160 (2020) 110085. doi:10.1016/j.matchar.2019.110085.

[41] Y. Song, G. Dai, J. Zhou, Z. Bian, L. Zhao, L. Song, Characterizing porous volume of cement-based concrete by multiscale image analysis, Journal of Materials in Civil Engineering 32 (9) (2020) 04020267. doi:10.1061/(ASCE)MT.1943-5533.0003355.

[42] C. Naber, F. Kleiner, F. Becker, L. Nguyen-Tuan, C. Rößler, M. A. Etzold, J. Neubauer, C-S-H pore size characterization via a combined nuclear magnetic resonance (NMR)–scanning electron microscopy (SEM) surface relaxivity calibration, Materials 13 (7) (2020) 1779. doi:10.3390/ma13071779.

[43] M. Neumann, J. Staněk, O. M. Pecho, L. Holzer, V. Beneš, V. Schmidt, Stochastic 3D modeling of complex three-phase microstructures in SOFC-electrodes with completely connected phases, Computational Materials Science 118 (2016) 353–364. doi:10.1016/j.commatsci.2016.03.013.

[44] O. M. Pecho, O. Stenzel, B. Iwanschitz, P. Gasser, M. Neumann, V. Schmidt, M. Prestat, T. Hocker, R. J. Flatt, L. Holzer, 3D microstructure effects in Ni-YSZ anodes: Prediction of effective transport properties and optimization of redox stability, Materials 8 (9) (2015) 5554–5585. doi:10.3390/ma8095265.

[45] M. Neumann, R. Cabiscol, M. Osenberg, H. Markötter, I. Manke, J. H. Finke, V. Schmidt, Characterization of the 3D microstructure of Ibuprofen tablets by means of synchrotron tomography, Journal of Microscopy 274 (2) (2019) 102–113. doi:10.1111/jmi.12789.

[46] O. Furat, T. Leißner, K. Bachmann, J. Gutzmer, U. Peuker, V. Schmidt, Stochastic modeling of multidimensional particle properties using parametric copulas, Microscopy and Microanalysis 25 (3) (2019) 720–734. doi:10.1017/S1431927619000321.

[47] EN 197-1, Cement - Part 1: Composition, specifications and conformity criteria for common cements (2011).

[48] S. E. Rasheeduzzafar, A. S. Hussain, Al-Gahtani, Pore solution composition and reinforcement corrosion characteristics of microsilica blended cement concrete, Cement and Concrete Research 21 (1991) 1035–1048. doi:10.1016/0008-8846(91)90064-O.

[49] V. Kocaba, E. Gallucci, K. L. Scrivener, Methods for determination of degree of reaction of slag in blended cement pastes, Cement and Concrete Research 42 (3) (2012) 511 – 525. doi:10.1016/j.cemconres.2011.11.010.

[50] A. Baldermann, Y. Fleischhacker, S. Schmidthaler, K. Wester, M. Nachtnebel, S. Eichinger, Removal of barium from solution by natural and iron(III) oxide-modified allophane, beidellite and zeolite adsorbents, Materials 13 (11) (2020) 2582. doi:10.3390/ma13112582.

[51] K. L. Scrivener, Backscattered electron imaging of cementitious microstructures: understanding and quantification, Cement and Concrete Composites 26 (8) (2004) 935 – 945. doi:10.1016/j.cemconcomp.2004.02.029.

[52] B. Münch, L. Holzer, Contradicting geometrical concepts in pore size analysis attained with electron microscopy and mercury intrusion, Journal of the American Ceramic Society 91 (12) (2008) 4059–4067. doi:10.1111/j.1551-2916.2008.02736.x.

[53] L. Holzer, D. Wiedenmann, B. Münch, L. Keller, M. Prestat, P. Gasser, I. Robertson, B. Grobéty, The influence of constrictivity on the effective transport properties of porous layers in electrolysis and fuel cells, Journal of Materials Science 48 (7) (2013) 2934–2952. doi:10.1007/s10853-012-6968-z.

[54] W. Burger, M. J. Burge, Digital Image Processing: An Algorithmic Introduction Using Java, Springer, 2016.

[55] A. Buades, B. Coll, J. Morel, A non-local algorithm for image denoising, in: 2005 IEEE Computer Society Conference on Computer Vision and Pattern Recognition (CVPR'05), Vol. 2, 2005, pp. 60–65. doi:10.1109/CVPR.2005.38.

[56] H. Wong, M. Head, N. Buenfeld, Pore segmentation of cement-based materials from backscattered electron images, Cement and Concrete Research 36 (6) (2006) 1083 – 1090. doi:10.1016/j.cemconres.2005.10.006.

[57] F. Deschner, B. Münch, F. Winnefeld, B. Lothenbach, Quantification of fly ash in hydrated, blended portland cement pastes by backscattered electron imaging, Journal of Microscopy 251 (2) (2013) 188–204. doi:10.1111/jmi.12061.

[58] D. Legland, I. Arganda-Carreras, P. Andrey, Morpholibj: integrated library and plugins for mathematical morphology with ImageJ, Bioinformatics 32 (22) (2016) 3532–3534. doi:10.1093/bioinformatics/btw413.

[59] F. Gong, D. Zhang, E. Sicat, T. Ueda, Empirical estimation of pore size distribution in cement, mortar, and concrete, Journal of Materials in Civil Engineering 26 (7) (2014) 04014023. doi:10.1061/(ASCE)MT.1943-5533.0000945.

[60] J. Ohser, K. Schladitz, 3D Images of Materials Structures: Processing and Analysis, J. Wiley & Sons, 2009.

[61] M. Rafiei, S. Löhr, A. Baldermann, R. Webster, C. Kong, Quantitative petrographic differentiation of detrital vs diagenetic clay minerals in marine sedimentary sequences: Implications for the rise of biotic soils, Precambrian Research 350 (2020) 105948. doi:10.1016/j.precamres.2020.105948.

[62] L. Held, D. S. Bové, Applied Statistical Inference, Springer, 2014.

[63] N. L. Johnson, S. Kotz, N. Balakrishnan, Continuous Univariate Distributions, Vol. 1, J. Wiley & Sons, 1994.

[64] N. L. Johnson, S. Kotz, N. Balakrishnan, Continuous Univariate Distributions, Vol. 2, J. Wiley & Sons, 1995.

[65] M. Nakagami, The m-distribution—a general formula of intensity distribution of rapid fading, in: W. Hoffman (Ed.), Statistical Methods in Radio Wave Propagation, Pergamon, 1960, pp. 3 – 36. doi:10.1016/B978-0-08-009306-2.50005-4.

[66] K. Leschonski, W. Alex, B. Koglin, Teilchengrößenanalyse. 1. Darstellung und Auswertung von Teilchengrößenverteilungen (Fortsetzung), Chemie Ingenieur Technik 46 (3) (1974) 101–106. doi:10.1002/cite.330460307.

[67] U. Frank, S. E. Wawra, L. Pflug, W. Peukert, Multidimensional particle size distributions and their application to nonspherical particle systems in two dimensions, Particle & Particle Systems Characterization 36 (7) (2019) 1800554. doi:10.1002/ppsc.201800554.

[68] H. Justnes, J. Skocek, T. A. Østnor, C. J. Engelsen, O. Skjølsvold, Microstructural changes of hydrated cement blended with fly ash upon carbonation, Cement and Concrete Research 137 (2020) 106192. doi:j.cemconres.2020.106192.

[69] J. Juhart, G. A. David, C. Nickel, G. Fischer, F. Mittermayr, A new combined filler concept for eco-concrete, in: H. Toivonen, S. Colton, M. Cook, D. Ventura (Eds.), Proc. of 14th International Congress on the Chemistry of Cement (ICCC 2015), Beijing, 2015.

[70] J. Wang, D. Niu, R. Ma, Y. Zhang, Investigation of sulfate attack resistance of shotcrete under dry-wet cycles, Journal of Wuhan University of Technology-Mater. Sci. Ed. 31 (6) (2016) 1329–1335. doi:10.1007/s11595-016-1535-0.

[71] F. Steindl, I. Galan, A. Baldermann, M. Sakoparnig, L. Briendl, J. Juhart, M. Thumann, M. Dietzel, R. Röck, W. Kusterle, F. Mittermayr, Sulfate durability and leaching behaviour of dry- and wet-mix shotcrete mixes, Cement and Concrete Research 137 (2020) 106180. doi:10.1016/j.cemconres.2020.106180.